

Transport Induced by Mean-Eddy Interaction: II. Analysis of Transport Processes

Kayo Ide^a and Stephen Wiggins^b

^a*Department of Atmospheric and Oceanic Science,
Center for Scientific Computation and Mathematical Modeling,
Institute for Physical Science and Technology,
& Earth System Science Interdisciplinary Center,
University of Maryland, College Park, USA*

^b*School of Mathematics, University of Bristol, Bristol BS8 1TW, UK*

Abstract

We present a framework for the analysis of transport processes resulting from the mean-eddy interaction in a flow. The framework is based on the **Transport Induced by the Mean-Eddy Interaction** (TIME) method presented in a companion paper [1]. The TIME method estimates the (Lagrangian) transport across stationary (Eulerian) boundaries defined by chosen streamlines of the mean flow. Our framework proceeds after first carrying out a sequence of preparatory steps that link the flow dynamics to the transport processes. This includes the construction of the so-called “instantaneous flux” as the Hovmöller diagram. Transport processes are studied by linking the signals of the instantaneous flux field to the dynamical variability of the flow. This linkage also reveals how the variability of the flow contributes to the transport. The spatio-temporal analysis of the flux diagram can be used to assess the efficiency of the variability in transport processes. We apply the method to the double-gyre ocean circulation model in the situation where the Rossby-wave mode dominates the dynamic variability. The spatio-temporal analysis shows that the inter-gyre transport is controlled by the circulating eddy vortices in the fast eastward jet region, whereas the basin-scale Rossby waves have very little impact.

Key words: Eulerian Transport, Lagrangian Transport, Mean-Eddy Interaction, Dynamical Systems Approach, Wind-Driven Ocean Circulation

PACS: 47.10.Fg, 47.11.St, 47.27.ed, 47.51.+a, 92.05.-x, 92.10.A-, 92.10.ab, 92.10.ah, 92.10.ak, 92.10.Lq, 92.10.Ty, 92.60.Bh

Email addresses: ide@umd.edu (Kayo Ide), S.Wiggins@bris.ac.uk (Stephen Wiggins).

URLs: <http://www.atmos.umd.edu/~ide> (Kayo Ide),
<http://www.maths.bris.ac.uk/people/faculty/maxsw/> (Stephen Wiggins).

Contents

1	Introduction	3
2	Building the links between variability and transport	6
2.1	Mean flow	6
2.2	Dynamic variability of the flow in $\mathbf{u}'(\mathbf{x}, t)$	7
2.3	Flux variability of $\phi(\mathbf{x}, t)$	8
2.4	Boundary curve C and parameterization of the reference trajectory	10
2.5	Flux diagram	10
3	The TIME functions and the graphical approach to the analysis of transport processes	12
3.1	The accumulation function	12
3.2	The displacement function	14
4	Application to the Inter-gyre Transport in the Double-Gyre Ocean	15
5	Concluding remarks	18
	References	21
	Tables	22
	Figures	24

1 Introduction

Analysis of geophysical flows often employs techniques that decompose the velocity field in a manner that will yield a desired insight [2]. A commonly used technique is the mean-eddy decomposition

$$\mathbf{u}(\mathbf{x}, t) = \overline{\mathbf{u}}(\mathbf{x}) + \mathbf{u}'(\mathbf{x}, t) , \quad (1a)$$

$$Q(\mathbf{x}, t) = \overline{Q}(\mathbf{x}) + Q'(\mathbf{x}, t) , \quad (1b)$$

where the field is described by the unsteady eddy activity around a mean state; henceforth, $\{\cdot\}$ and $\{\cdot\}'$ denote the time average (mean) and the residual (unsteadiness or eddy), respectively. Here $\mathbf{u} = (u_1, u_2)^T$ is the velocity field and Q represents any property of the flow such as temperature, chemical or biological properties. In the absence of unsteadiness, the kinematic transport occurs only along the mean streamlines on which $\overline{\mathbf{u}}(\mathbf{x})$ is everywhere tangent. An effect of the unsteadiness is to stir the flow instantaneously and induce mixing across the mean streamlines over time. It is also well accepted that instantaneous pictures of the unsteady flow themselves do not indicate transport explicitly.

A variety of Eulerian and Lagrangian methods have been developed to study transport observationally, analytically, and numerically. The companion paper [1] presented a new transport method that is a hybrid combination of Lagrangian and Eulerian methods. This paper develops a framework for the analysis and diagnosis of transport processes based on this new method. Our main focus is on two-dimensional geophysical flows that may be compressible. To introduce our method, we begin with a brief discussion of Lagrangian and Eulerian methods specific to our needs.

The basis of any Lagrangian method involves the tracking of individual fluid particles by solving the initial value problem of $\frac{d}{dt}\mathbf{x} = \mathbf{u}(\mathbf{x}, t)$. Starting from \mathbf{x}_0 at time t_0 , a particle trajectory $\mathbf{x}(t; \mathbf{x}_0, t_0)$ at time t is given by the temporal integral of the local velocity field along itself:

$$\mathbf{x}(t; \mathbf{x}_0, t_0) - \mathbf{x}_0 = \int_{t_0}^t \mathbf{u}(\mathbf{x}(\tau; \mathbf{x}_0, t_0), \tau) d\tau . \quad (2)$$

A very rudimentary description of Lagrangian transport may be obtained from a so-called “spaghetti diagram” which is constructed by simply plotting the trajectories. Typically this results in a complex tangle of curves from which detailed a detailed assessment of Lagrangian transport may prove difficult. In recent years the mathematical theory of dynamical systems has provided a new point of view and tools for classifying, organizing, and analyzing detailed

and complex trajectory information by providing a theoretical and computational framework for an understanding of the geometric properties of “flow structures”. Recent reviews of the dynamical systems approach to transport are given in [3,4,5].

Nevertheless, there still remain many challenging problems to be tackled by Lagrangian methods. Quantifying Lagrangian transport is extremely elaborate in general. While techniques based on dynamical systems theory are conceptually ideal for tracking transport of fluid particles, they have not proven as useful for studying transport of Q , unless Q is uniform and passive. Moreover, Lagrangian methods are not suitable for separating and/or isolating the roles played by the mean state $\bar{\mathbf{u}}(\mathbf{x})$ and the unsteadiness $\mathbf{u}'(\mathbf{x}, t)$ in the trajectory $\mathbf{x}(t; \mathbf{x}_0, t_0)$.

In contrast to Lagrangian methods, transport quantities computed with Eulerian methods utilize information taken at pre-selected stationary points. At a station $\bar{\mathbf{x}}^E$, the most basic Eulerian transport may be given by the temporal integral of the local velocity during a time interval $[t_0, t_1]$:

$$\int_{t_0}^{t_1} \mathbf{u}(\bar{\mathbf{x}}^E, t) dt = (t_1 - t_0) \bar{\mathbf{u}}(\bar{\mathbf{x}}^E) . \quad (3)$$

The resulting transport is associated with $\bar{\mathbf{u}}(\mathbf{x})$, but not $\mathbf{u}'(\mathbf{x}, t)$ by default [compare with (2) for the Lagrangian case]. For transport across a stationary Eulerian curve $E = \{\bar{\mathbf{x}}^E(p)\}$ where p is a parameter along E , the total transport during $[t_0, t_1]$ over a spatial segment $[p_A, p_B]$ is

$$\int_{t_0}^{t_1} \int_{p_A}^{p_B} \frac{d}{dp} \bar{\mathbf{x}}^E(p) \wedge \mathbf{u}(\bar{\mathbf{x}}^E(p), t) dp dt = (t_1 - t_0) \int_{p_A}^{p_B} \frac{d}{dp} \bar{\mathbf{x}}^E(p) \wedge \bar{\mathbf{u}}(\bar{\mathbf{x}}^E(p)) dp$$

An advantage of the Eulerian methods is the ability to compute the transport of Q as well, by replacing $\mathbf{u}(\mathbf{x}, t)$ with $Q(\mathbf{x}, t)\mathbf{u}(\mathbf{x}, t)$. Overtime, the Eulerian methods gives $\overline{Q(\mathbf{x}, t)\mathbf{u}(\mathbf{x}, t)} = \overline{Q(\mathbf{x})\bar{\mathbf{u}}(\mathbf{x})} + \overline{Q'(\mathbf{x}, t)\mathbf{u}'(\mathbf{x}, t)}$. Hence, the Eulerian methods account for the statistical contribution to transport at the second-order.

Our new transport method [1] has the unique ability to identify the effects of the mean-eddy interaction in a way that neither Lagrangian nor Eulerian methods have accomplished. This advantage that comes from blending of the Lagrangian and Eulerian approaches. The method uses information on a stationary (Eulerian) boundary curve C to estimate (Lagrangian) transport of both fluid particles and Q across C without requiring tracking of individual fluid particles. The method estimates the transport by integrating the instantaneous effects of the unsteady flux while taking the particle advection of the

mean flow into account. We refer to our method that quantifies the **T**ransport **I**nduced by the **M**ean-**E**ddy interaction as “TIME.”

By construction, the TIME method offers a framework for a detailed analysis of the spatio-temporal structure of transport processes. The goal of this paper is to present this framework through a study of the inter-gyre transport processes in a wind driven, three-layer quasi-geostrophic ocean model (Figure 1). Due to its relevance to the mid-latitude ocean circulation, the dynamics of wind-driven double-gyre ocean models have been actively studied from various points of view over the last few decades (for review, see [6] and references therein).

[Fig.1]

Although the details of transport are highly dependent on the dynamics of the flows, there are five common preparatory steps for the analysis using the TIME method. The initial two steps of the five concern obtaining an understanding of the flow dynamics based on the mean-eddy decomposition (1). The first step is to examine the global flow structure given by the mean flow $\bar{\mathbf{u}}(\mathbf{x})$, which we call the *reference state* (Figure 1a for the wind-driven ocean; see Section 2.1 for the details). The second step is to understand the nature of the unsteady eddy activity in $\mathbf{u}'(\mathbf{x}, t)$. Unsteady eddy activity is also referred to as the *variability*. In geophysical flows, variability is often associated with the temporal evolution of the spatially coherent structures (Figure 1b; see Section 2.2 for the details). It should be clear that these coherent structures are defined in the instantaneous Eulerian field and different from the so-called “Lagrangian coherent structures” [7].

With understanding and insights of the mean and the variability at hand, the third step is to compute the instantaneous flux that stirs the flow. The instantaneous flux is expressed naturally in terms of a “mean-eddy interaction”. (Figure 1c for the wind-driven ocean; see Section 2.3).

The fourth step is to select the *Eulerian boundary*, C , of interest based on the mean flow structure. Any mean streamline with reasonable length can be a potential C . The actual choice of C should be left up to the specific geophysical interests. In Figure 1a we show our choice of C for the intergyre transport in the wind-driven ocean; which we discuss further in Section 2.4).

The last step is to extract the information of the instantaneous flux on C . The signals of the variability in the mean-eddy interaction are conveniently represented by a space-time diagram (i.e., *the Hovmöller diagram*), which we call the *flux diagram* to emphasize its role in the TIME method (see Section 2.5).

An important outcome of the five preparatory steps is that they link the flow dynamics to the transport processes, and *vice versa*, in terms of the mean-eddy interaction. This link, and the spatio-temporal integration employed by the TIME method, comprise the foundation for the graphical approach to the

study of the transport processes (see Section 3). In the double-gyre application, the analysis will reveal how/when/where the circulating eddy vortices in a localized area over the eastward jet are responsible for the inter-gyre transport, whereas the basin-scale Rossby waves play a very small role (see Section 4). We use the same flow field as in [1] that is nearly periodic in time and has a heteroclinic connection in the mean. It is worth noting that the TIME method does not require either of such conditions (i.e., presence of the time periodicity and the heteroclinic connection).

The outline of the paper is as follows. Section 2 presents the preparatory steps using the application to the inter-gyre transport in the double-gyre wind-driven ocean circulation. We extend the TIME functions defined by [1] and present a graphical approach that facilitates the analysis of transport processes in Section 3. Inter-gyre transport processes in the double-gyre ocean are analyzed in Section 4. Section 5 summarizes the results and provides a discussion.

2 Building the links between variability and transport

In this section we define the five preparatory steps mentioned in the previous section in detail and carry them out in the context of the analysis of inter-gyre transport in a wind driven double-gyre ocean circulation model. The flow field is obtained by numerical simulation of a three-layer quasi-geostrophic model with the model parameters chosen to be consistent with the mid-latitude, wind-driven ocean circulations [6,8]. As a result of a constant wind-stress curl 0.165dyn/cm^2 applied at the ocean surface, the basin-scale circulation fluctuates almost periodically around the mean state with dominant spectral peak at period $T \approx 151\text{days}$ after the initial 30,000-day spin-up from the rest. For our analysis time starts after this spin-up. In this study, we analyze the inter-gyre transport processes in the top layer. The instantaneous flow patterns are given by the streamfunction $\psi(\mathbf{x}, t)$ that is related to the velocity $\mathbf{u}(\mathbf{x}, t)$ by $\mathbf{u}(\mathbf{x}, t) = (-\frac{\partial}{\partial y}, \frac{\partial}{\partial x})\psi(\mathbf{x}, t)$.

2.1 Mean flow

Given $\bar{\mathbf{u}}(\mathbf{x})$, the corresponding streamfunction $\bar{\psi}(\mathbf{x})$ is the reference state that provides a geometrical structure of the global flow. Figure 1a shows $\bar{\psi}(\mathbf{x})$ for the double-gyre circulation in which the axis of the eastward jet divides the ocean basin into two gyres. Because the ocean model has gone through the pitchfork bifurcation prior to the Hopf bifurcation [6] (in terms of increasing wind-stress curl), an asymmetry exists between the cyclonic subpolar

gyre and the anticyclonic subtropical gyre. At the confluence of the southward and northward western boundary currents, the cyclonic subpolar gyre and anti-cyclonic subtropical gyre form an asymmetric dipole (along \mathbf{x}_J and \mathbf{x}_N indicated by the diamonds in Figure 1a). We refer to this region as the “dipole region.” The eastward jet defined between the center of the subpolar vortex and that of the subtropical gyre carries the mean net transport $\bar{\psi}_{NT} \equiv |\bar{\psi}_{sp} - \bar{\psi}_{st}| = 24028$, where $\bar{\psi}_{sp}$ (< 0) is the minimum $\bar{\psi}(\mathbf{x})$ over the subpolar vortex and $\bar{\psi}_{st}$ (> 0) is the maximum over the subtropical vortex. The asymmetry of the two gyres is measured by the transport difference, [9] $\bar{\psi}_{TD} \equiv |\bar{\psi}_{sp}| - |\bar{\psi}_{tr}| = 5438$.

2.2 Dynamic variability of the flow in $\mathbf{u}'(\mathbf{x}, t)$

An understanding of the eddy activity (variability) in $\mathbf{u}'(\mathbf{x}, t)$ is the key for the analysis of transport processes using the TIME method. In the double-gyre application, the model ocean dynamics is almost periodic in time resulting from the Rossby-wave mode [6,8]. In the left panel of Figure 2, the evolution of the ocean dynamics is shown by two time series. The net transport of the jet $NT(t) \equiv |\psi_{sp}(t) - \psi_{st}(t)|/\bar{\psi}_{NT}$ normalized by the mean state net transport $\bar{\psi}_{NT}$ indicates the fluctuation of the jet strength around the mean. The transport difference $TD(t) = (|\psi_{sp}(t)| - |\psi_{st}(t)|)/\bar{\psi}_{TD}$ normalized by $\bar{\psi}_{TD}$ measures the fluctuation of the asymmetry between the subpolar and subtropical gyres around the mean. Here $\psi_{sp}(t)$ is the minimum $\psi(\mathbf{x}, t)$ over the subpolar gyre and $\psi_{st}(t)$ is the maximum over the subtropical gyre. The two time series show that the amplitude of the fluctuation is of the order smaller than 0.1 with respect to the mean. This fact is important since the validity of the TIME functions requires the fluctuations to be small compared to the mean.

For convenience, we define the period of the k -th ocean oscillation by $T^{[k]} = [t_{38}^* + (k-1)T, t_{38}^* + kT)$ starting from t_{38}^* when a minimum of $NT(t)$ occurs first time after the spin-up; the number in the subscript of t^* represents time in day from here on. We also define $T^{[k.1]}$ and $T^{[k.2]}$ as the first and the second half of $T^{[k]}$, respectively. During $T^{[k.1]}$, $NT(t)$ increases from a minimum to a maximum while $TD(t)$ reaches a minimum after about $T/4$. Conversely during $T^{[k.2]}$, $NT(t)$ decreases while $TD(t)$ reaches a maximum after about $3T/4$ from the beginning of $T^{[k]}$.

[Fig.2]

The eddy streamfunction field $\psi'(\mathbf{x}, t)$ associated with $\mathbf{u}'(\mathbf{x}, t)$ provides an instantaneous pattern of the eddy activity. In the double-gyre application, $\psi'(\mathbf{x}, t)$ shows two types of eddy activity (Figure 1b). One is the westward propagation of Rossby waves, whose latitudinally elongated structures are especially visible in the eastern basin. Typically there are three waves in the en-

tire basin, although the one in the western basin is distorted around the dipole region. The travel time of the wave from the eastern to the western boundary is 453(=151×3)days. Each wave has the longitudinal width 333(=1000/3)km and travels with the propagation phase speed 2.2(=1000/453)km/day.

As mentioned briefly in the introduction, for our study of inter-gyre transport in the wind-driven ocean, the axis of the eastward jet is chosen to be C . It is the separatrix that connects the western boundary to the eastern boundary. We will discuss this in more detail in Section 2.4.

Although the westward propagation of Rossby waves is seen in almost the entire ocean basin, the dipole region has the eddy activity that is more energetic. The left panels of Figure 3 show the phases of these eddy vortices during $T^{[7]}$ that starts at t_{944}^* . At $t_{944}^* + T/4(= t_{982}^*)$ when $TD(t)$ is minimum (corresponding to Figure 1b), a strongly positive eddy vortex is located near \mathbf{x}_1 . This eddy vortex weakens as the center moves from \mathbf{x}_1 along C as shown at $t_{944}^* + T/2(= t_{1020}^*)$ when $NT(t)$ is maximum. It intensifies once again as the center reaches \mathbf{x}_2 as shown at $t_{944}^* + 3T/4(= t_{1058}^*)$ when $TD(t)$ is maximum. It moves further along C as shown at $t_{944}^* + T$ later ($t_{944}^* + T = t_{1095}^*$), until the center leaves C near \mathbf{x}_N as shown at t_{982}^* for $5T/4$ later ($t_{944}^* + 5T/4(= t_{1131}^*)$). And it continues to make a cyclic rotation around the sub-polar vortex. One cyclic rotation takes $2T$. The negative eddy vortex located in the west of this positive eddy vortex at $t_{944}^* + T/4$ follows the same cyclic motion but $T/2$ behind with the opposite phase of $NT(t)$ and $TD(t)$ with respect to the positive eddy vortex.

[Fig.3]

This cyclic rotation of the eddy vortices is far from uniform because the eddy vortices tend to pulsate, i.e., when they intensify during $T^{[k.1]}$ or $T^{[k.2]}$ (e.g., $t_{944}^* + T/4$ or $t_{944}^* + 3T/4$ in Figure 3), the centers hardly move; when they weaken at the end of $T^{[k.1]}$ or $T^{[k.2]}$ (e.g., t_{944}^* or $t_{944}^* + T/2$), the centers move very quickly. As we shall see below, this complexity in the flow dynamics strongly influences the inter-gyre transport processes. We emphasize that these eddy vortices are not Lagrangian, i.e., particles don't move with them.

These two types of eddy activity, westward propagation of the Rossby wave and cyclonic circulation of the eddy vortices, are synchronized. In particular they merge in the eastern part of the dipole region. At $t_{944}^* + T/4$, a negative eddy vortex connects to a negative half of the Rossby wave around \mathbf{x}_3 as shown in Figures 1 and 3. This merger occurs every $T/2$ and is associated with the alternating sign of $\psi'(\mathbf{x}, t)$.

2.3 Flux variability of $\phi(\mathbf{x}, t)$

The instantaneous flux across the mean flow

$$\phi(\mathbf{x}, t) \equiv \bar{\mathbf{u}}(\mathbf{x}) \wedge \mathbf{u}'(\mathbf{x}, t) \quad (5)$$

is explicitly defined in terms of the “mean-eddy interaction” induced by the instantaneous spatial interaction of $\bar{\mathbf{u}}(\mathbf{x})$ and $\mathbf{u}'(\mathbf{x}, t)$. Geometrically, $\phi(\mathbf{x}, t)$ is the signed area of the parallelogram defined by $\bar{\mathbf{u}}(\mathbf{x})$ and $\mathbf{u}'(\mathbf{x}, t)$ with the unit of $\phi(\mathbf{x}, t)$ being flux per unit time over the length $|\bar{\mathbf{u}}(\mathbf{x})|$. The amplitude of $\phi(\mathbf{x}, t)$ depends not only $|\bar{\mathbf{u}}(\mathbf{x})|$ and $|\mathbf{u}'(\mathbf{x}, t)|$, but also on the angle between $\bar{\mathbf{u}}(\mathbf{x})$ and $\mathbf{u}'(\mathbf{x}, t)$. We refer to the coherent structures associated with $\phi(\mathbf{x}, t)$ as the *flux zones*.

In the double-gyre application, the two types of eddy activity in $\mathbf{u}'(\mathbf{x}, t)$ lead to distinct evolution of flux zones in $\phi(\mathbf{x}, t)$. In the eastern basin where the Rossby waves dominate the variability, the direction change of $\bar{\mathbf{u}}(\mathbf{x})$ in both gyres breaks the wave structure latitudinally into three flux zones with alternating signs (Figure 1c). Near the jet axis, a sequence of the Rossby waves lead to a sequence of flux zones with alternating signs; the positive flux zones correspond to northward flux, while the negative ones correspond to the southward flux. The width and the westward propagation speed of these flux zones are the same as those of the Rossby waves in $\psi'(\mathbf{x}, t)$.

In the dipole region where $\bar{\mathbf{u}}(\mathbf{x})$ is stronger and non-uniform while $\mathbf{u}'(\mathbf{x}, t)$ consists of the cyclic rotation of the four circulating eddy vortices, the mean-eddy interaction is complex (Figure 3). Most significantly, the eddy vortices along the jet lead to the flux zones with the alternating signs that are visible particularly where $|\bar{\mathbf{u}}(\bar{\mathbf{x}}^C(s))|$ is large along the mean jet axis. These flux zones in $\phi(\mathbf{x}, t)$ pulsate in sync with the eddy vortices in $\psi'(\mathbf{x}, t)$ (compare the right panels of Figure 3 with the left panels). The shapes of the flux zones are more loosely defined than those of the eddy vortices due to the spatially nonlinear interference by $\bar{\mathbf{u}}(\mathbf{x})$. As the circulating eddy vortices intensify when $TD(t)$ is minimum ($t_{944}^* + T/4$) or maximum ($t_{944}^* + 3T/4$), three relatively well-defined flux zones are visible over $[\mathbf{x}_J, \mathbf{x}_1]$, $[\mathbf{x}_1, \mathbf{x}_2]$, and $[\mathbf{x}_2, \mathbf{x}_N]$ between the eddy vortex centers with the middle one stronger than the other two. In between consecutive intensifications, the flux zones weaken and quickly propagate along C as $NT(t)$ reaches minimum (t_{944}^*) or maximum ($t_{944}^* + T/2$). The propagation speed and direction of the three flux zones are the same as those of the circulating eddy vortices.

As the eddy vortex leaves the mean jet axis near at \mathbf{x}_N , a weak fourth flux zone is generated over $[\mathbf{x}_N, \mathbf{x}_3]$ that propagate towards the upstream of the mean flow. Because the eddy vortices and the Rossby waves merge around \mathbf{x}_3 over $[\mathbf{x}_N, \mathbf{x}_S]$, the flux zones associated with them also merge there.

2.4 Boundary curve C and parameterization of the reference trajectory

The TIME method uses the streamlines associated with $\bar{\mathbf{u}}(\mathbf{x})$ as the Eulerian boundaries C across which the transport is estimated. Along C , the flight-time s is a natural choice of the coordinate variable because $C = \{\bar{\mathbf{x}}^C(s)\}$ is obtained by solving for $\frac{d}{ds}\bar{\mathbf{x}}^C(s) = \bar{\mathbf{u}}(\bar{\mathbf{x}}^C(s))$ with a choice of initial position $\bar{\mathbf{x}}^C(0)$. Particle advection along C in the mean flow is referred to as the *reference trajectory*. Starting from $\bar{\mathbf{x}}^C(s_0)$ at t_0 , the reference trajectory is uniquely parameterized by $s_0 - t_0$ and can be written as $(s, t) = (s_0 - t_0 + t, t)$ using the flight-time coordinate.

Some key locations on C are shown in Figure 1. In $\bar{\psi}(\mathbf{x})$, \mathbf{x}_J is the location that is far enough from the hyperbolic stagnation point of C on the western boundary point in s so that $\bar{\mathbf{u}}(\mathbf{x}_J)$ becomes non-negligible to induce the instantaneous flux; \mathbf{x}_N and \mathbf{x}_S are the locations where the (meandering) jet axis makes sharp turns. In $\psi'(\mathbf{x}, t)$, \mathbf{x}_1 and \mathbf{x}_2 are the locations where the centers of the eddy vortices pause to intensify; \mathbf{x}_N is where the eddy centers leave C ; around \mathbf{x}_3 , two types of variability, the circulating eddy vortices in the upstream and the Rossby waves in the downstream, meet on C . Accordingly, \mathbf{x}_J , \mathbf{x}_1 , \mathbf{x}_2 , \mathbf{x}_N and \mathbf{x}_3 are the boundary points of the flux zones along C in $\phi'(\mathbf{x}, t)$ as the eddy vortices pause to intensify and meet the Rossby waves in $\phi(\mathbf{x}, t)$. The flight-time coordinates of \mathbf{x}_J , \mathbf{x}_1 , \mathbf{x}_2 , \mathbf{x}_N , \mathbf{x}_3 , and \mathbf{x}_S are $s_J = 110$, $s_1 = 114.5$, $s_2 = 118.5$, $s_N = 129$, $s_3 = 150$, and $s_S = 174.5$ in the unit of days, respectively, starting with $\bar{\mathbf{x}}^C(0) = (2 \times 10^{-38} \text{km}, 1011.8 \text{km})$ located very close to the western boundary.

2.5 Flux diagram

The Hovmöller diagram [10,11] of the instantaneous flux in the (s, t) space:

$$\mu^C(s, t) \equiv \phi(\bar{\mathbf{x}}^C(s), t) = \bar{\mathbf{u}}(\bar{\mathbf{x}}^C(s)) \wedge \mathbf{u}'(\bar{\mathbf{x}}^C(s), t) \quad (6)$$

is fundamental to the TIME method because it contains the stirring information locally and instantaneously extracted from $\phi(\mathbf{x}, t)$ along C . We refer to it as the *flux diagram*. At a given instance t , a continuous segment of s with $\mu^C(s, t) > 0$ corresponds to a positive flux zone where the instantaneous flux goes from the right to the left across C with respect to the direction of increasing s . The direction of the flux is reversed for $\mu^C(s, t) < 0$. The reference trajectory $(s, t) = (s_0 - t_0 + t, t)$ is a diagonal line going through (s_0, t_0) with the unit slope (see the main panel of Figure 2).

The nature of the signals in $\mu^C(s, t)$ is dependent on both the system and the

choice of C . These signals can be complex, as we shall observe in the double-gyre application (Figure 2). Nonetheless, having systematically examined the mean $\bar{\mathbf{u}}(\mathbf{x})$ (in terms of $\bar{\psi}(\mathbf{x})$; Section 2.1), dynamic variability $\mathbf{u}'(\mathbf{x}, t)$ (in terms of $\psi'(\mathbf{x}, t)$; Section 2.2), flux variability $\phi(\mathbf{x}, t)$ (Section 2.3), and the geographic location of C in the flow field (Section 2.4), the physical interpretation of the signals in $\mu^C(s, t)$ is straightforward. Any signals can be traced back to certain flux zones in $\phi(\mathbf{x}, t)$, and hence the mean-eddy interaction process between $\bar{\mathbf{u}}(\mathbf{x})$ and $\mathbf{u}'(\mathbf{x}, t)$.

By the construction of the flux diagram along C , the propagation speed and direction of the signals in $\mu^C(s, t)$ are defined with respect to the particle advection along the reference trajectory of the mean flow. Signals with positive slopes correspond to the downstream propagation of the coherent structures in $\psi'(\mathbf{x}, t)$. In contrast, signals with negative slopes are related to the upstream propagation of the coherent structures. If the slope is steeper than 1, then the propagation speed is slower than the particle advection along C in $\bar{\psi}(\mathbf{x})$.

In the double-gyre application, $\mu^C(s, t)$ is almost periodic with period T (Figure 2), i.e., $\mu^C(s, t) = \mu^C(s, t + T)$, due to the periodic dynamics in $\psi'(\mathbf{x}, t)$. Within one period, the positive and negative phases are almost anti-symmetric, i.e., $\mu^C(s, t) \approx -\mu^C(s, t + T/2)$. For $s < s_J$, $\mu^C(s, t)$ is very small because of near-zero $\bar{\mathbf{u}}(\bar{\mathbf{x}}^C(s))$ and changes the sign in synchrony with $T^{[k,1]}$ for $\mu^C(s, t) > 0$ and $T^{[k,2]}$ for $\mu^C(s, t) < 0$.

The strongest signals in $\mu^C(s, t)$ are concentrated over the segment $[s_J, s_N]$ where the mean jet in $\bar{\psi}(\mathbf{x})$ is fast and the circulating eddy vortices in $\psi'(\mathbf{x}, t)$ are energetic. Due to the pulsation of the circulating eddy vortices as they propagate along C (Section 2.3), the corresponding flux zones also pulsate simultaneously over the three consecutive segments, $S_a \equiv [s_J, s_1)$, $S_b \equiv [s_1, s_2)$, and $S_c \equiv [s_2, s_N)$, with the alternating signs of $\mu^C(s, t)$. The widths of S_a , S_b , and S_c are narrow (6.5, 4, and 10.5days, respectively) with respect to the period of intensification $T/2$ (75.5days) during which the flux zones hardly move. Thus the slopes of the dominant signals in $\mu^C(s, t)$ are steep. At the end of $T^{[k,1]}$ and $T^{[k,2]}$, these flux zones weaken and quickly propagate downstream to the next segment along C . A positive flux zone over S_a during $T^{[k,1]}$ connects to S_b during $T^{[k,2]}$, and then to S_c during $T^{[k+1,1]}$ in a sequence; conversely a negative flux zone over S_a during $T^{[k,2]}$ moves over to S_b during $T^{[k+1,1]}$, and then to S_c during $T^{[k+1,2]}$. Over the subsequent segment $S_d \equiv [s_N, s_3)$ along C , weak signals of the circulating eddy vortices are observed in $\mu^C(s, t)$. The slope is negative over S_d because of the upstream propagation of the circulating eddies as their centers leave C around \mathbf{x}_N (Figure 3).

The westward propagation of the Rossby waves is seen for $s > s_3$. The slope is negative and less than 1 because the Rossby waves propagate against the mean flow with the propagation speed faster than the particle advection along C .

Magnitude of $\mu^C(s, t)$ rapidly decays to zero for $s > 500$ because of extremely small $|\bar{\mathbf{u}}(\bar{\mathbf{x}}^C(s))|$ and $|\mathbf{u}'(\bar{\mathbf{x}}^C(s), t)|$ there (not shown). The change in the propagation slope over $s \in [200\text{day}, 240\text{day}]$ is mainly caused by the meander of C (Figure 1). Over $S_e \equiv [s_S, s_N)$, the signals of the Rossby waves and those of the circulating eddy vortices are mixed because the two types of variability merge between \mathbf{x}_N and \mathbf{x}_S in $\psi'(\mathbf{x}, t)$ (Sections 2.2 and 2.3).

Accordingly, the (s, t) space can be divided into sub-domains based on the types of the mean-eddy interaction. Table 1 summarizes the main domains for the double-gyre application. Two types of the variability are associated with the two domains; D^{cv} where the signals are associated with the circulating eddy vortices in the dipole region and D^{rw} where the signals are associated with the Rossby wave in the downstream region of the eastward jet. The total domain is $D^{\text{all}} = D^{\text{cv}} \cup D^{\text{rw}}$. Temporally periodic variability leads to the temporal decomposition of D^{all} based on $T^{[k]}$, i.e., $D^{\text{all}} = \cup D^{[k]}$. Another useful definition D is transient $D(t)$ that covers the (s, t) space up to the present time t .

[Tab.1]

3 The TIME functions and the graphical approach to the analysis of transport processes

The companion paper [1] introduced the TIME functions. The main focus in [1] was the mathematical formulation, the validity of perturbation approximations, as well as the verification of the method by comparing with the Lagrangian method based on the lobe dynamics for the case of C chosen as a heteroclinic connection of the reference state. This section refines the TIME functions for a much more detailed analysis of the transport processes due to the variability in the flow. We note that although the TIME functions as developed in [1] are based on a perturbation approach in the sense that the fluctuating part of the velocity field is "small" compared to the reference state, none of the development up to this point in the paper requires this smallness requirement—all that has been required is the decomposition of the velocity field into a (steady) reference state and a fluctuation about the reference state.

3.1 The accumulation function

The accumulation function along C is defined as

$$m^C(s, t; t_0 : t_1) = \int_{t_0}^{t_1} \mu^C(s - t + \tau, \tau) d\tau . \quad (7)$$

The left-hand side of (7) denotes the amount of fluid transport that occurs during the accumulation time interval $[t_0, t_1]$ evaluated at (s, t) . The right-hand side of (7) expresses the transport in terms of the spatio-temporal integration of $\mu^C(s-t+\tau, \tau)$ during $t_0 \leq \tau \leq t_1$. Thus it can be thought that accumulation is advected, while it may continue to occur, with the reference trajectory going through (s, t) . The sign of $m^C(s, t; t_0 : t_1)$ corresponds to the direction of transport across C ; $m^C(s, t; t_0 : t_1) > 0$ is from right to left across C ; the direction of the flux is reversed for $m^C(s, t; t_0 : t_1) < 0$.

The basic idea of (7) is that the transport can be estimated just for the time period of interest $[t_0, t_1]$. It can be extended to study “when”, “where”, and how” variability of the flow contributes to the transport. This is done by restricting the integration in (7) to a specific space-time domain D that contains the particular signals of interest (Section 2.5). Formally and practically this leads to the slight modification to the accumulation function:

$$m^C(s, t; D) = \int H(s-t+\tau, \tau; D) \mu^C(s-t+\tau, \tau) d\tau, \quad (8a)$$

where

$$H(s-t+\tau, \tau; D) = \begin{cases} 1 & \text{if } (s-t+\tau, \tau) \in D, \\ 0 & \text{otherwise} \end{cases} \quad (8b)$$

acts as a switch to turn on and off the instantaneous flux depending on whether or not $(s-t+\tau, \tau)$ is in D at time τ . For example using $D(t)$ as D , $m^C(s, t; D(t))$ is the transient transport by accounting for the accumulation up to the present time t (see Table 1 for the definition of $D(t)$).

For the analysis of transport processes, there are properties of $m^C(s, t; D)$ that are useful (see [1] for technical details). One is the *invariance* property along the individual reference trajectory by advection of the accumulation:

$$m^C(s, t; D) = m^C(s + \delta, t + \delta; D) \quad (9)$$

for any δ , but with D fixed. The invariance property implies a conservation law of the accumulation by the advection. At any (s, t) along a reference trajectory, $m^C(s, t; D)$ is independent of t as long as D is independent of t .

The other useful property is the (*piece-wise*) *independence* property of D . By breaking up the domain D into L non-overlapping sub-domains D_1, \dots, D_L , the piece-wise independence property implies that the accumulation function can be written as

$$m^C(s, t; D) = \sum_{l=1}^L m^C(s, t; D^l) . \quad (10)$$

For example, in the double-gyre application, the effect of the circulating eddy vortices and that of the Rossby wave propagation can be examined separately, while the overall transport is the sum of the two, i.e., $m^C(s, t; D^{\text{all}}) = m^C(s, t; D^{\text{cv}}) + m^C(s, t; D^{\text{rw}})$. Transient transport can be also decomposed into the sub-domains as long as t is the same for all, e.g., $m^C(s, t; D^{\text{all}}(t)) = \sum_k m^C(s, t; D^{[k]}(t))$.

A key feature of the TIME method is the *graphical approach* using the Hovmöller diagram of $\mu^C(s, t)$. By definition (8), transport processes are described by the manner in which the reference trajectory passes through the signals in $\mu^C(s, t)$ over the specific domain of interest D (see Figure 2). Conversely, it discloses the dynamical origins of $m^C(s, t; D)$ by relating the signals in $\mu^C(s, t)$ to dynamic activities in $\mathbf{u}'(\mathbf{x}, t)$ through $\phi(\mathbf{x}, t)$ (Section 2). Thus, the graphical approach unveils the dynamical processes of the mean-eddy interaction that are responsible for transport.

Moreover, the graphical approach can assess the efficiency of the dynamic activity $\mathbf{u}'(\mathbf{x}, t)$ in contributing to $m^C(s, t; D)$. The accumulation is, in general, extremely efficient if a signal in $\mu^C(s, t)$ propagates with the same unit slope because it keeps accumulating the same signed instantaneous flux. In other words, transport processes are the most efficient if the (Eulerian) eddy activity in $\psi'(\mathbf{x}, t)$ propagates at the same speed as the (Lagrangian) particle advection of the mean flow $\bar{\psi}(\mathbf{x})$ along C . In contrast, if the eddy activity is temporally periodic and propagates upstream of the mean flow, then the net contribution to the accumulation adds up to zero. This is because the reference trajectory cuts across the signals of $\mu^C(s, t)$ whose sign alternates periodically, resulting in the cancellation of the accumulation.

3.2 The displacement function

The second type of TIME function quantifies the geometry associated with transport, up to the leading-order in the “size” of the unsteady part of the velocity field. To describe the geometry in the two-dimensional flow, we use an orthogonal coordinate set (l, r) for \mathbf{x} near C , where the arc-length coordinate $l = l^C(s)$ of $\bar{\mathbf{x}}^C(s)$ is defined along C by $\frac{d}{ds}l^C(s) = |\bar{\mathbf{u}}(\bar{\mathbf{x}}^C(s))|$. By taking the normal projection $\bar{\mathbf{x}}^C(s)$ of \mathbf{x} onto C , the signed distance coordinate $r = r^C(l^C(s))$ is defined by $r^C(l^C(s)) \equiv (\bar{\mathbf{u}}(\bar{\mathbf{x}}^C(s))/|\bar{\mathbf{u}}(\bar{\mathbf{x}}^C(s))|) \wedge (\mathbf{x} - \bar{\mathbf{x}}^C(s))$, where $|\bar{\mathbf{u}}(\bar{\mathbf{x}}^C(s))| \neq 0$. If $r^C(l^C(s)) > 0$, then \mathbf{x} lies in the left side of C with respect to the direction defined by the direction of increasing s . The side of \mathbf{x} is reversed for $r^C(l^C(s)) < 0$.

The displacement distance function is defined as

$$r^C(l^C(s), t; D) = \frac{a^C(s, t; D)}{|\bar{\mathbf{u}}(\bar{\mathbf{x}}^C(s))|}, \quad (11a)$$

where

$$a^C(s, t; D) = \int H(s - t + \tau, \tau; D) \bar{e}^C(s - t + \tau : s) \mu^C(s - t + \tau, \tau) d\tau \quad (11b)$$

is the displacement area per unit s and H is defined in (8b). Compressibility of the flow is taken into account by

$$\bar{e}^C(s - t + \tau : s) = \exp \left\{ \int_{s-t+\tau}^s D_{\mathbf{x}} \mathbf{u}(\bar{\mathbf{x}}^C(\sigma)) d\sigma \right\}, \quad (11c)$$

so that the flux that has occurred at $(s - t + \tau, \tau)$ may expand or compress as it advects to (s, t) with the reference particle advection. If the mean flow is incompressible as in the quasi-geostrophic model used for the double-gyre application, then $m^C(s, t; D)$ and $a^C(s, t; D)$ are the same since $\bar{e}^C(s - t + \tau : s) \equiv 1$ holds for any $s - t + \tau$ and s . The technical details can be found in [1].

The advantage of $r^C(l, t; D)$ is that it gives the geometry of the so-called ‘‘pseudo-lobes’’ that represent the spatial coherency of the transport. Pseudo-lobes are the chain-like geometry of transport defined by the areas surrounded by $C = \{(l, r) \mid r = 0\}$ and the curve $\{(l, r) \mid r = r^C(l, t; D)\}$ at a given time t . A positive pseudo-lobe corresponds to a coherent area defined by $\{(l, r) \mid 0 \leq r \leq r^C(l, t; D)\}$, while a negative pseudo-lobe is a coherent area defined by $\{(l, r) \mid r^C(l, t; D) \leq r \leq 0\}$. The relation of the pseudo-lobes to the Lagrangian lobes is discussed in [1].

4 Application to the Inter-gyre Transport in the Double-Gyre Ocean

Having carried out the preparatory steps (Section 2) and defined the TIME functions (Section 3), we now use the TIME method to analyze inter-gyre transport processes in the the double-gyre circulation. We focus on the following three aspects of transport processes using the specific types of sub-domain D for $m^C(s, t; D)$ (see Table 1 for the definition of these sub-domains): using $D(t)$, we study how the variability give rise to the development of the pseudo-lobes; using $D^{\text{cv}}(t)$ and $D^{\text{rw}}(t)$, we compare the impact of the circulating eddy vortices and that of the Rossby waves to the inter-gyre transport; using D^{all}

along with $D(t)$ and $D^{[k]}$, we analyze the inter-gyre transport processes of the Lagrangian lobes and examine the impact of variability during $T^{[k]}$. We also use $m^C(s, t; D)$ in place for $a^C(l, t; D)$, with which we describe the geometry $r^C(l, t; D)$ associated with the transport, particular in terms of the pseudo-lobes.

Figure 4 shows the transient accumulation $m^C(s, t; D(t))$ in the Hovmöller diagram from the past up to the evaluation (present) time t as t progresses upward. Due to the nearly periodic variability in $\psi'(\mathbf{x}, t)$, $m^C(s, t; D(t))$ is also nearly periodic in t , i.e., $m^C(s, t; D(t)) = m^C(s, t + T; D(t + T))$. Because of the anti-symmetry in the oscillation, $m^C(s, t; D(t))$ is also anti-symmetric with respect to a $T/2$ -shift in t , i.e., $m^C(s, t; D(t)) = -m^C(s, t + T/2; D(t + T/2))$. For $s < s_J$ at any t , $m^C(s, t; D(t))$ is nearly zero because hardly any accumulation happens in the upstream direction of s_J due to extremely small $\mu^C(s, t)$ there. For $s > s_S$, $m^C(s, t; D(t)) \approx m^C(s + \delta, t + \delta; D(t + \delta))$ along the reference trajectory (e.g., diagonal line in Fig 4) with $\delta > 0$ indicates very little accumulation there. It suggests that the Rossby waves contribute very little to the inter-gyre transport in the downstream direction of s_S .

[Fig.4]

By a comparison of Figure 4 with Figure 2, accumulation processes in $m^C(s, t; D(t))$ are closely related to the evolution of the flux zones in $\mu^C(s, t)$ (Section 2.5). Below, we follow the development of a positive pseudo-lobe in Figure 4 starting from $T^{[7.1]}$ as t progresses. This pseudo-lobe first gains positive accumulation over S_a where a positive flux zone pulsates during $T^{[7.1]}$. If there is no flux in the downstream of S_a (i.e., $\mu^C(s, t) = 0$ for $s > s_1$), then this positive pseudo-lobe will spread over $[s_J, s_1 + T/2]$ at the end of $T^{[7.1]}$ because the accumulation is simply advected along the reference trajectory; this corresponds to the invariance property (9). However, positive accumulation that occurs over S_a is canceled shortly after it is advected into S_b where a strong negative flux zone pulsates during $T^{[7.1]}$. Hence, a small, narrow (in terms of s) positive pseudo-lobe develops mostly over S_a during $T^{[7.1]}$. At the end of $T^{[7.1]}$ when the positive flux zone over S_a moves quickly to S_b , the positive pseudo-lobe follows it. In Figure 5, $m^C(s, t; D(t))$ at $t = t_{944}^* + T/2$ is shown by the dashed line and this positive pseudo-lobe is indicated by $T/2$.

[Fig.5]

During $T^{[7.2]}$, the positive pseudo-lobe continues to develop over S_b where the positive flux zone pulsates with large amplitude. Because this flux zone is stronger than any flux zones, the pseudo-lobe slowly spreads into the downstream region by the advection of the accumulation. At the end of $T^{[7.2]}$ when the positive flux zone quickly moves to S_c , the positive pseudo-lobe once again follows it. In Figure 5, $m^C(s, t; D(t))$ is plotted at $t = t_{944}^* + T$ by the solid line. The spread of the pseudo-lobe is observed over S_d .

During $T^{[8.1]}$, the pseudo-lobe continues to develop over S_c where the positive flux zone pulsates before disappearing at s_N . It also continues to spread into

the downstream region because the flux zones are much weaker there. Speed of the spread increases in the downstream direction of s_3 because of a weaker, positive flux zone induced by the Rossby waves over S_e . At the same time, the spread of the negative pseudo-lobe that started in $T^{[7.2]}$ gradually pushes this positive pseudo-lobe from the upstream region. At the end of $T^{[8.1]}$, the main part of the positive pseudo-lobe is located over S_e (Figure 5).

During $T^{[8.2]}$, the positive pseudo-lobe first gains accumulation from a positive flux zone induced by the Rossby waves over S_e , but loses it quickly because the negative flux zone induced by the Rossby waves moves into S_e . In the meantime, the positive pseudo-lobe continues to spread into the downstream region. Once the accumulation passes s_S , it simply advects along the reference trajectory. Near the end of $T^{[8.2]}$, the positive pseudo-lobe reaches the final form as the entire pseudo-lobe passes s_S .

Our analysis of $m^C(s, t; D(t))$ therefore reveals that the majority of inter-gyre transport occurs over a very limited segment $[s_J, s_S]$. Accumulation processes are synchronized with the evolution of the circulating eddy vortices, and are fed mostly by the three flux zones over $3T/2$ in t while they are mostly the same signed over the spatial segments S_a through S_c ; in the subsequent $T/2$ in t , the Rossby waves help form the final shape of the pseudo-lobe with the width $T/2$ in s . After $2T$ in t , the pseudo-lobe moves by the advection along the reference trajectory because there are no further accumulation in the downstream direction of S_S . Thus, it takes almost $2T$ in t to develop a fully-grown pseudo-lobe of the width $T/2$ in s . While developing, the propagation speed of the pseudo-lobe is much slower than the particle advection along the reference trajectory: over $2T$ in t , the pseudo-lobe moves about $T/2$ in s starting from S_a .

The analysis also reveals that the Rossby waves have very little impact on the inter-gyre transport for two reasons. One reason is that the signals of $\mu^C(s, t)$ in D^{rw} are weak (see Section 2.5). The other reason comes from the fact that the upstream propagation of the signal in $\mu^C(s, t)$ in D^{rw} is nearly periodic in time (see Section 3.1). Figure 6 shows the decomposition of the transient inter-gyre transport $m^C(s, t; D(t))$ into the part induced by the circulating eddy vortices $m^C(s, t; D^{cv}(t))$ and that induced by the Rossby waves $m^C(s, t; D^{rw}(t))$ at $t = t_{36}^* + kT$ (end of $T^{[k]}$), where $m^C(s, t; D(t)) = m^C(s, t; D^{cv}(t)) + m^C(s, t; D^{rw}(t))$ by the piece-wise independence property (10). By the definition of D^{rw} , $m^C(s, t; D^{rw}(t)) = 0$ for $s < s_3$ means that the Rossby waves impact the inter-gyre transport only in the downstream of s_3 (dash-dot line). The amount of accumulation, $m^C(s, t; D^{rw}(t))$, is small except over $[s_3, s_S]$ where the signals of the circulating eddy vortices and that of the Rossby waves are mixed in $\mu^C(s, t)$ (Section 2.5).

[Fig.6]

Lagrangian lobes have proven to be extremely useful and insightful in a va-

riety of transport studies and they provide precise amounts of Lagrangian transport of fluid [12,4,5,3]. In the companion paper [1], it was shown that $m^C(s, t; D^{\text{all}})$ provides a good approximation to the amount of transport carried by individual lobes in the inter-gyre transport (see also [13]). Figure 7 shows $m^C(s, t; D^{\text{all}})$ by the dash line at the end of $T^{[k]}$. It is doubly periodic in s and t because of the periodic dynamics in $\psi'(\mathbf{x}, t)$.

Using the TIME method, we analyze the transport processes associated with the Lagrangian lobes. The transient transport $m^C(s, t; D(t))$ in the past up to the present time t is shown in Figure 7 by the solid line. By the piece-wise independence (10), the difference $m^C(s, t; D^{\text{all}}) - m^C(s, t; D(t))$ corresponds to the transport that will occur in the future of t . A significant difference is observed mainly for $s < s_N$ where $m^C(s, t; D(t))$ does not include the active accumulation over $[s_J, s_N]$ yet. A slight difference occurs over $[s_N, s_J + T]$ due to the flux zones of the Rossby waves there. For $s > s_J + T$, $m^C(s, t; D^{\text{all}})$ and $m^C(s, t; D(t))$ are almost indistinguishable, suggesting that no further transport will occur in the future over the segment of C . Once again we confirm that the impact of Rossby waves in the downstream region is negligible for inter-gyre transport. Note that $m^C(s, t; D^{\text{cv}}) \approx m^C(s, t; D^{\text{cv}}(t))$ and $m^C(s, t; D^{\text{rw}}) \approx m^C(s, t; D^{\text{rw}}(t))$ hold over there as well (see Figure6).

[Fig.7]

To examine how much transport occurs during one period $T^{[k]}$ of the unsteady eddy activity in $\psi'(\mathbf{x}, t)$, Figure 7 shows $m^C(s, t; D^{[k]})$ by the dash-dot line. Over $[s_J, s_J + T]$ of the length T in s , $m^C(s, t; D^{[k]})$ and $m^C(s, t; D(t))$ are almost indistinguishable because both include the active accumulation over $[s_J, s_N]$. Accordingly, during $T^{[k]}$, only one positive pseudo-lobe grows close to its final form over $[s_J + T/2, s_J + T]$ with width $T/2$ in s , but no negative pseudo-lobe can grow to the final form. If the period is shifted by $T/2$, then only one negative pseudo-lobe grows into its final form over the same $[s_J + T/2, s_J + T]$ segment. For $s > s_J + T$, $m^C(s, t; D^{[k]})$ differs from $m^C(s, t; D(t))$ because of the accumulation in $m^C(s, t; D(t))$ that has occurred prior to $T^{[k]}$.

5 Concluding remarks

Building on the transport method developed in the companion paper [1], we have formulated a framework for the analysis of the dynamical processes that influence transport. The transport method, called the “**T**ransport **I**nduced by the **M**ean-**E**ddy interaction” (TIME), is a hybrid combination of Lagrangian and Eulerian transport approaches. Our analysis proceeds by a step by step approach. In particular, the steps are to determine the mean flow structure of $\bar{\mathbf{u}}(\mathbf{x})$, determine the dynamic variability in $\mathbf{u}'(\mathbf{x}, t)$, construct the instantaneous stirring chart $\phi(\mathbf{x}, t) = \bar{\mathbf{u}}(\mathbf{x}) \wedge \mathbf{u}'(\mathbf{x}, t)$ induced by the mean-eddy interaction, choose an Eulerian boundary $C = \{\bar{\mathbf{x}}^C(s)\}$, and compute the flux

diagram $\mu^C(s, t) = \phi(\bar{\mathbf{x}}^C(s), t)$. The signals in $\mu^C(s, t)$ are define relative to the reference particle advection along C , which is a diagonal line in the Hovmöller diagram.

The fundamental constructions underlying the TIME method involve computing transport, either as accumulation $m^C(s, t; D)$ or displacement area $a^C(l, t; D)$ (which gives displacement distance $r^C(l, t; D)$), which rely on the spatio-temporal integration of $\mu^C(s, t)$. This provides the two-way link between the variability of the flow and the actual transport processes. It is a unique feature of the TIME method that neither the Eulerian nor Lagrangian methods alone can provide. These fundamentals also provides a platform for a novel graphical approach to the analysis of transport processes.

While transport is highly system dependent, there are some common features that can hold in general that we can understand from our graphical approach for the analysis of transport processes. For example, the accumulation is most effective if the signals in $\mu^C(s, t)$ propagate with the same unit slope as the reference trajectory, i.e., dynamic variability propagates with the particle advection in the mean flow. However, if the dynamic variability is temporally near periodic, and the signal has a negative slope, then the net effect would be almost zero. This may happen when the wave propagates upstream in the mean flow, like in the westward Rossby wave propagation in the double-gyre application. The role of variability in transport is analytically studied in [14] and is based on a related spatio-temporal scale analysis.

We have applied our framework to the analysis of intergyre transport processes in the double-gyre ocean circulation where the Rossby-wave mode dominates the dynamic variability with a period T . The spatio-temporal analysis shows that the intergyre transport is controlled by a complex rotation of eddy vortices in the fast eastward jet near the western boundary current. The emergence of the pseudo-lobes is synchronized with the circulating eddy vortices in $\mathbf{u}'(\mathbf{x}, t)$. Pseudo-lobes having alternating signed area emerge every $T/2$ to transport water across the mean jet axis between the subpolar and subtropical gyres, while each pseudo-lobe spends almost $2T$ over a very limited segment in the upstream dipole region to fully develop. During the development period, the pseudo-lobes propagate at a much slower speed than the reference particle advection. However, once fully developed, they propagate downstream of the mean jet axis at the same speed as the reference particle advection. The basin-scale Rossby wave has very little impact on the intergyre transport.

Acknowledgment

This research is supported by ONR Grant No. N00014-09-1-0418, (KI) and ONR Grant No. N00014-01-1-0769 (SW).

References

- [1] K. Ide, S. Wiggins, Transport induced by mean-eddy interaction: I. Theory and relation to Lagrangian lobe dynamics, submitted to *Physica D*.
- [2] J. Peixoto, A. Oort, *Physics of Climate*, progress in oceanography, vol.1, Edition, American Institute of Physics, 1992.
- [3] S. Wiggins, The dynamical systems approach to Lagrangian transport in oceanic flows, *Ann. Rev. Fluid Mech.* 37 (2005) 295–328.
- [4] A. Mancho, D. Small, S. Wiggins, A tutorial on dynamical systems concepts applied to Lagrangian transport in oceanic flows defined as finite time data sets: Theoretical and computational issues, *Phys. Rep.* 437 (2006) 55–124.
- [5] R. Samelson, S. Wiggins, *Lagrangian Transport in Geophysical Jets and Waves: The Dynamical Systems Approach*, Springer-Verlag, New York, 2006.
- [6] H. A. Dijkstra, *Nonlinear Physical Oceanography A Dynamical Systems Approach to the Large Scale Ocean Circulation and El Nino*, 2nd Edition, Springer, 2005.
- [7] G. Haller, Lagrangian coherent structures from approximate velocity data, *Phys. Fluids A* 14 (2002) 1851–1861.
- [8] E. Simonnet, M. Ghil, K. Ide, R. Temam, S. Wang, Low-frequency variability in shallow-water models of the wind-driven ocean circulation. part ii: Time-dependent solutions, *J. Phys. Oceanogr.* 33 (2003) 729–752.
- [9] K.-I. Chang, M. Ghil, K. Ide, C.-C. A. Lai, Transition to aperiodic variability in a wind-driven double-gyre circulation model, *J. Phys. Oceanogr.* 31 (2002) 1260–1286.
- [10] E. Hovmöller, The trough and ridge diagram, *Tellus* 1 (1949) 62–66.
- [11] O. Martis, C. Schwierz, H. C. Davies, A refined Hovmöller diagram, *Tellus* 58A (2006) 221–226.
- [12] N. Malhotra, S. Wiggins, Geometric structures, lobe dynamics, and Lagrangian transport in flows with aperiodic time dependence, with applications to Rossby wave flow, *J. Nonl. Sci.* 8 (1998) 401–456.
- [13] C. Coulliette, S. Wiggins, Intergyre transport in a wind-driven, quasigeostrophic double gyre: An application of lobe dynamics, *Nonl. Proc. Geophys.* 7 (2000) 59–85.
- [14] K. Ide, S. Wiggins, Role of variability in transport, in preparation.

List of Tables

- 1 Definition of the sub-domains for the double-gyre application. 23

Domain	Description	Definition
D^{cv}	domain associated with the circulating eddy vortices	$\{(s, t) \mid s < s_{\text{tr}}\}$
D^{rw}	domain associated with the Rossby wave propagation	$\{(s, t) \mid s \geq s_{\text{tr}}\}$
D^{all}	entire domain	$D^{\text{cv}} \cup D^{\text{rw}}$
$D^{[k]}$	domain for the k -th oscillation period	$\{(s, t) \mid t \in T^{[k]}\}$
$D(t)$	transient (with respect to present time t)	$\{(s, \tau) \mid \tau < t\}$
$D^{[k]}(t)$	transient (with respect to present time t) during the k -th oscillation period in $\mathbf{u}'(\mathbf{x}, t)$	$\{(s, \tau) \mid \tau < t \text{ and } \tau \in T^{[k]}\}$

Table 1

Definition of the sub-domains for the double-gyre application.

List of Figures

- 1 Wind-driven double-gyre circulation at wind-stress curl 0.165dyn/cm^2 : a) mean streamline field $\bar{\psi}(\mathbf{x})$ averaged over T with contour interval 2000; b) eddy streamline field $\psi'(\mathbf{x}, t)$ at $t = t_{944}^* + T/4 (= t_{982}^*)$ with contour interval 500; and c) instantaneous flux field $\phi(\mathbf{x}, t)$ at $t = t_{944}^* + T/4 (= t_{982}^*)$ with contour interval 50. (see also Figure 3). In all panels, the dashed contours correspond to the negative values in all panels the Eulerian boundary C for the inter-gyre transport shown by a thick solid line. In $\bar{\psi}(\mathbf{x})$, \mathbf{x}_J , \mathbf{x}_N , and \mathbf{x}_S are shown by the diamonds; In $\psi'(\mathbf{x}, t)$ and $\phi(\mathbf{x}, t)$, \mathbf{x}_1 , \mathbf{x}_2 , and \mathbf{x}_3 are shown by the triangles. The flight-time coordinates of \mathbf{x}_J , \mathbf{x}_1 , \mathbf{x}_2 , \mathbf{x}_N , \mathbf{x}_S and \mathbf{x}_3 are $s_{J=110}$, $s_1 = 114.5$, $s_2 = 118.5$, $s_N = 129$, $s_S = 174.5$ and $s_3 = 150$ days. 26

- 2 The flux diagram $\mu^C(s, t)$ of the intergyre transport along the mean jet axis C as the Hovmöller diagram with t runs vertically. The contour interval is $20 (\text{km}^2 / \text{day}^2)$ with the dashed lines representing negative values. On the abscissa, the locations of $s_{J=110}$, $s_N = 129$, and $s_S = 174.5$ are indicated by the diamonds, while $s_1 = 114.5$, $s_2 = 118.5$, and $s_3 = 150$ are indicated by the triangles. In $\mu^C(s, t)$, $D^{[7]}$ are indicated by the two horizontal lines (solid) at $t = t_{944}^*$ and $t = t_{944}^* (= t_{1095}^*)$, while the boundary between D^{cv} and D^{rw} is shown by the vertical line (dashed) at $s = s_3$. The two diagonal lines (solid) are examples of the reference trajectory, i.e., $(s_0 - t_0 + t, t)$ with $(s_0, t_0) = (s_J, 900)$ and $(s_0, t_0) = (250, 900)$. The left panel shows $NT(t)$ (solid line) and $TD(t)$ (dashed line) vs. t . The top panel shows $|\bar{\mathbf{u}}(\bar{\mathbf{x}}^C(s))|$ vs. s with the same abscissa as $\mu^C(s, t)$. 27

- 3 The four phases of $\psi'(\mathbf{x}, t)$ (left) and $\phi(\mathbf{x}, t)$ (right) during $T^{[7]}$ at t_{944}^* when $NT(t)$ is minimum $t_{944}^* + T/4 (= t_{982}^*)$ when $TD(t)$ is minimum, $t_{944}^* + T/2 (= t_{1020}^*)$ when $NT(t)$ is maximum, and $t_{944}^* + 3T/4 (= t_{1058}^*)$ when $TD(t)$ is maximum with time increasing upward. The contour intervals are the same as in Figure 1b for $\psi'(\mathbf{x}, t)$ and Figure 1c for $\phi(\mathbf{x}, t)$. The solid line with the diamonds and triangles is C : from the upstream, the diamonds show \mathbf{x}_J , \mathbf{x}_N , and \mathbf{x}_S ; the triangles show \mathbf{x}_1 , \mathbf{x}_2 , and \mathbf{x}_3 as shown in Figure 1c. 28

- 4 Transient accumulation $m^C(s, t; D(t))$. The contour interval is 50 with the dashed contours for the negative values; the diamonds show s_J , s_N , and s_S while the triangles show s_1 , s_2 , and s_3 from upstream to downstream. A reference trajectory is plotted for $(s, t) = (s_0 - t_0 + t, t)$ that goes through s_S at the end of $T^{[7]}$ with $(s_0, t_0) = (s_S, t_{944}^* + T)$. 29
- 5 Pseudo-lobes of $m^C(s, t; D(t))$ at the end of $T^{[k.1]}$ ($t = t_{36}^* + (k - 1/2)T$; dash line) and at the end of $T^{[k.2]}$ ($t_{36}^* + kT$; solid line) for $k \geq 1$; the figure is made using $k = 7$. The positive pseudo-lobe that starts developing from the beginning of $T^{[7.1]}$ at t_{944}^* ($= t_{36}^* + (k - 1)T$ with $k = 7$) is indicated by: $T/2$ at $t = t_{944}^* + T/2$; T at $t = t_{944}^* + T$; $3T/2$ at $t_{944}^* + 3T/2$; and $2T$ at $t_{944}^* + 2T$. Dark diamonds show s_J , s_N , and s_S ; dark triangles show s_1 , s_2 , and s_3 ; lighter diamonds show $s_J + T$, $s_N + T$, and $s_S + T$; and light triangles show $s_1 + T$, $s_2 + T$, and $s_3 + T$. 30
- 6 Pseudo-lobes of $m^C(s, t; D(t))$ for the total transient transport (solid line; same as in Figure 5), $m^C(s, t; D^{cv}(t))$ by the circulating eddy vortices (dash line), and $m^C(s, t; D^{rw}(t))$ by the circulating eddy vortices (dash-dot line) at $t = t_{36}^* + kT$ (i.e., the end of $T^{[k]}$); the figure is made at t_{1095}^* using $k = 7$. Dark diamonds and dark triangles are the same as in Figure 5. 31
- 7 Pseudo-lobes of $m^C(s, t; D(t))$ for the total transient transport (solid line; same as in Figures 5), $m^C(s, t; D^{[k]})$ for transport induced during $T^{[k]}$ (dash-dot line), $m^C(s, t; D^{all})$ for total transport (dash line) at $t = t_{36}^* + kT$ (i.e., the end of $T^{[k]}$); the figure is made at t_{1095}^* using $k = 7$. Diamonds and triangles are the same as in Figure 5. 32

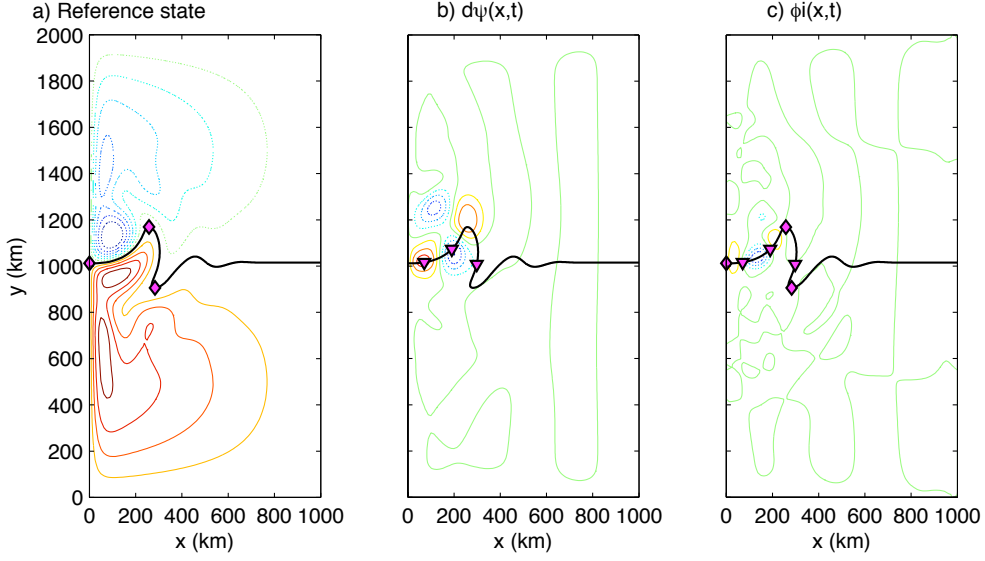


Fig. 1. Wind-driven double-gyre circulation at wind-stress curl 0.165 dyn/cm^2 : a) mean streamline field $\bar{\psi}(\mathbf{x})$ averaged over T with contour interval 2000; b) eddy streamline field $\psi'(\mathbf{x}, t)$ at $t = t_{944}^* + T/4 (= t_{982}^*)$ with contour interval 500; and c) instantaneous flux field $\phi(\mathbf{x}, t)$ at $t = t_{944}^* + T/4 (= t_{982}^*)$ with contour interval 50. (see also Figure 3). In all panels, the dashed contours correspond to the negative values in all panels the Eulerian boundary C for the inter-gyre transport shown by a thick solid line. In $\bar{\psi}(\mathbf{x})$, \mathbf{x}_J , \mathbf{x}_N , and \mathbf{x}_S are shown by the diamonds; In $\psi'(\mathbf{x}, t)$ and $\phi(\mathbf{x}, t)$, \mathbf{x}_1 , \mathbf{x}_2 , and \mathbf{x}_3 are shown by the triangles. The flight-time coordinates of \mathbf{x}_J , \mathbf{x}_1 , \mathbf{x}_2 , \mathbf{x}_N , \mathbf{x}_S and \mathbf{x}_3 are $s_{J=110}$, $s_1 = 114.5$, $s_2 = 118.5$, $s_N = 129$, $s_S = 174.5$ and $s_3 = 150$ days.

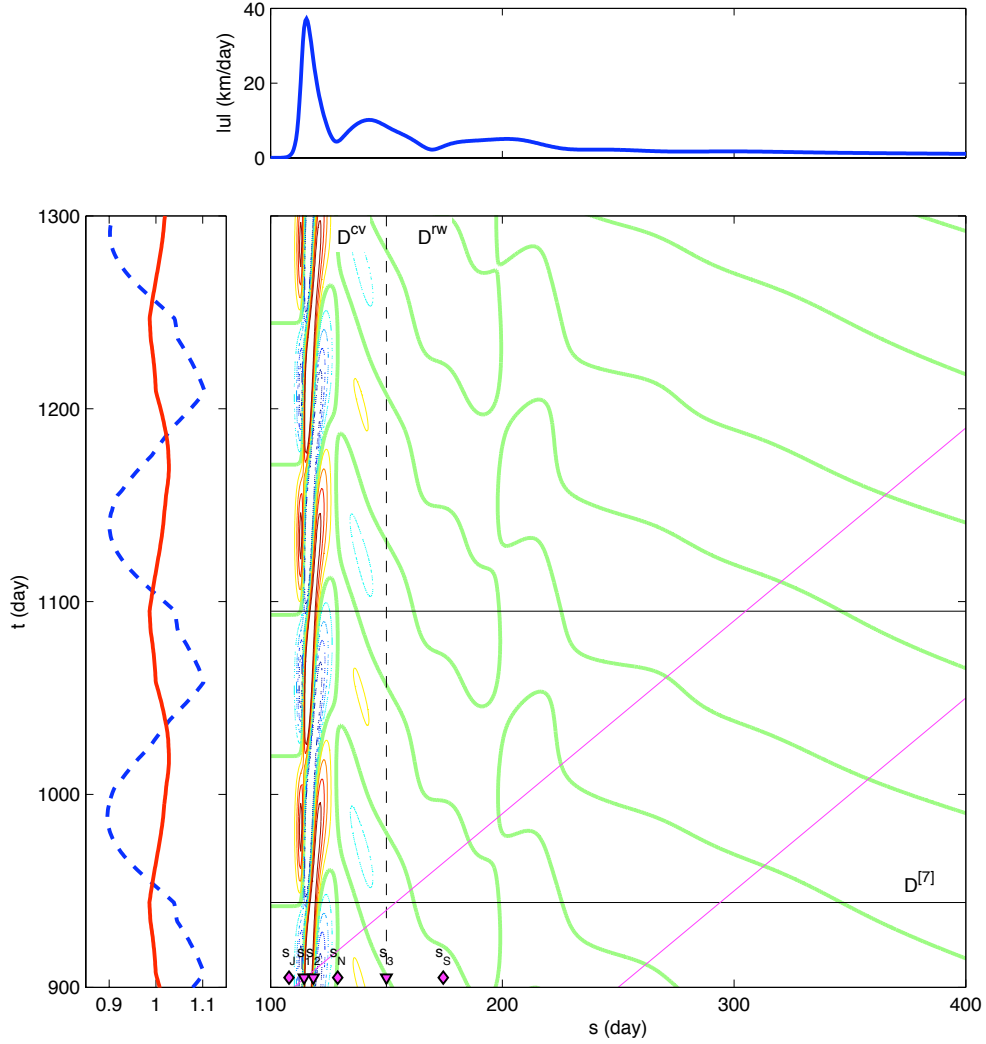


Fig. 2. The flux diagram $\mu^C(s, t)$ of the intergyre transport along the mean jet axis C as the Hovmöller diagram with t runs vertically. The contour interval is 20 ($\text{km}^2 / \text{day}^2$) with the dashed lines representing negative values. On the abscissa, the locations of $s_{J=110}$, $s_N = 129$, and $s_S = 174.5$ are indicated by the diamonds, while $s_1 = 114.5$, $s_2 = 118.5$, and $s_3 = 150$ are indicated by the triangles. In $\mu^C(s, t)$, $D^{[7]}$ are indicated by the two horizontal lines (solid) at $t = t_{944}^*$ and $t = t_{944}^* (= t_{1095}^*)$, while the boundary between D^{cv} and D^{rw} is shown by the vertical line (dashed) at $s = s_3$. The two diagonal lines (solid) are examples of the reference trajectory, i.e., $(s_0 - t_0 + t, t)$ with $(s_0, t_0) = (s_J, 900)$ and $(s_0, t_0) = (250, 900)$. The left panel shows $NT(t)$ (solid line) and $TD(t)$ (dashed line) vs. t . The top panel shows $|\bar{\mathbf{u}}(\bar{\mathbf{x}}^C(s))|$ vs. s with the same abscissa as $\mu^C(s, t)$.

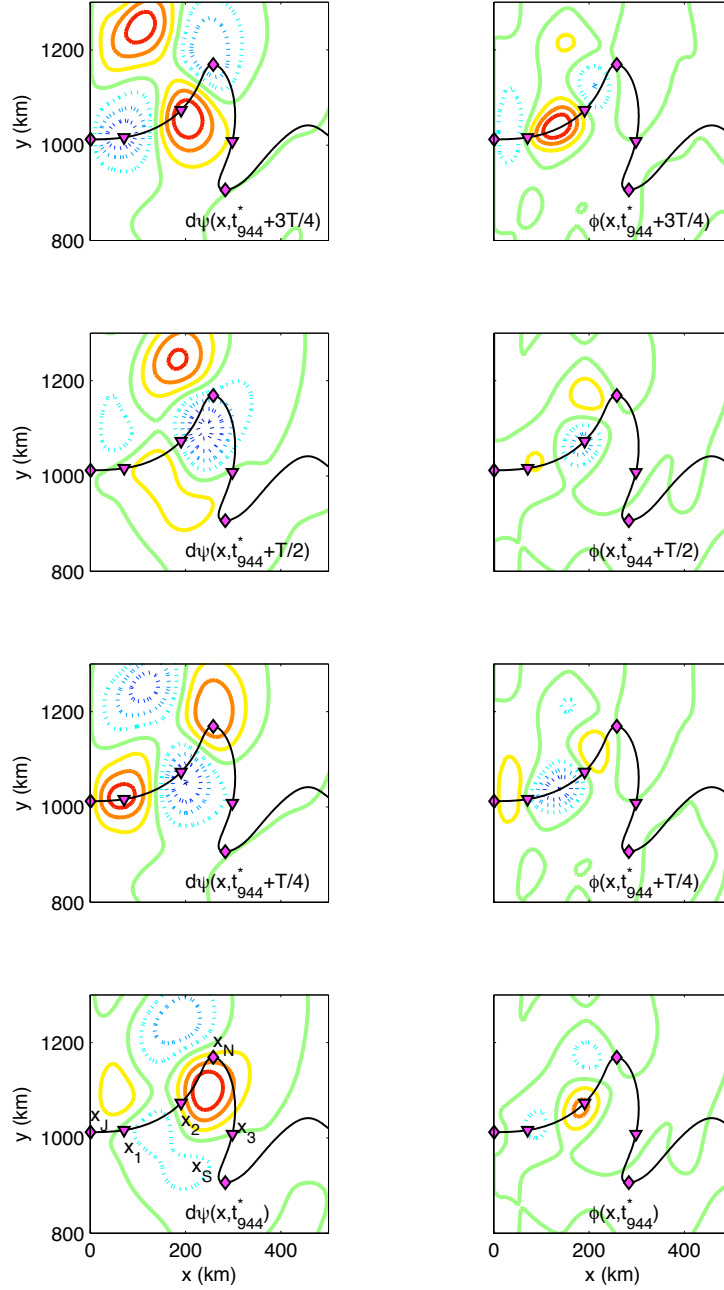


Fig. 3. The four phases of $\psi'(\mathbf{x}, t)$ (left) and $\phi(\mathbf{x}, t)$ (right) during $T^{[7]}$ at t_{944}^* when $NT(t)$ is minimum $t_{944}^* + T/4 (= t_{982}^*)$ when $TD(t)$ is minimum, $t_{944}^* + T/2 (= t_{1020}^*)$ when $NT(t)$ is maximum, and $t_{944}^* + 3T/4 (= t_{1058}^*)$ when $TD(t)$ is maximum with time increasing upward. The contour intervals are the same as in Figure 1b for $\psi'(\mathbf{x}, t)$ and Figure 1c for $\phi(\mathbf{x}, t)$. The solid line with the diamonds and triangles is C : from the upstream, the diamonds show \mathbf{x}_J , \mathbf{x}_N , and \mathbf{x}_S ; the triangles show \mathbf{x}_1 , \mathbf{x}_2 , and \mathbf{x}_3 as shown in Figure 1c.

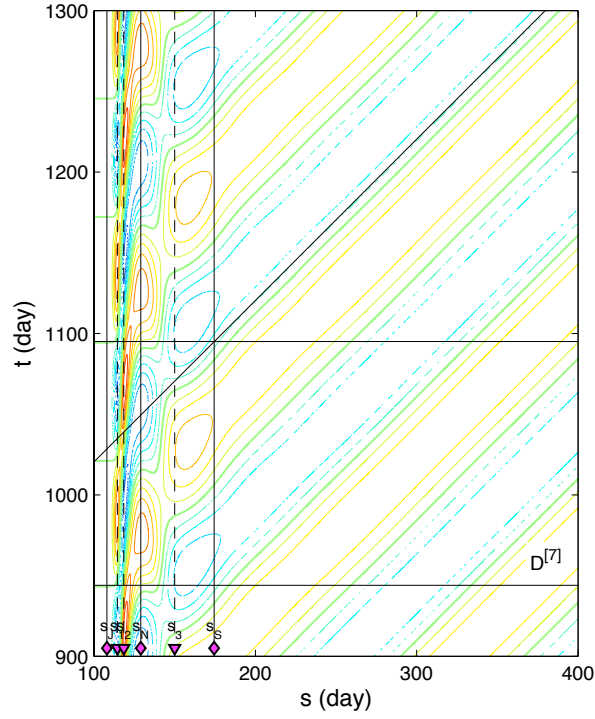


Fig. 4. Transient accumulation $m^C(s, t; D(t))$. The contour interval is 50 with the dashed contours for the negative values; the diamonds show s_J , s_N , and s_S while the triangles show s_1 , s_2 , and s_3 from upstream to downstream. A reference trajectory is plotted for $(s, t) = (s_0 - t_0 + t, t)$ that goes through s_S at the end of $T^{[7]}$ with $(s_0, t_0) = (s_S, t_{944}^* + T)$.

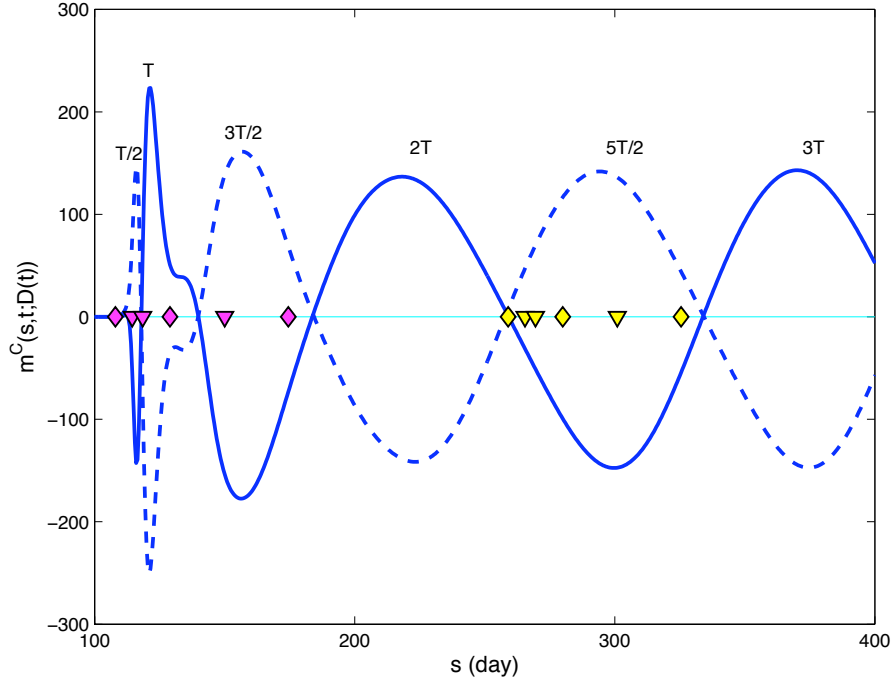


Fig. 5. Pseudo-lobes of $m^C(s, t; D(t))$ at the end of $T^{[k.1]}$ ($t = t_{36}^* + (k - 1/2)T$; dash line) and at the end of $T^{[k.2]}$ ($t_{36}^* + kT$; solid line) for $k \geq 1$; the figure is made using $k = 7$. The positive pseudo-lobe that starts developing from the beginning of $T^{[7.1]}$ at $t_{944}^* (= t_{36}^* + (k - 1)T$ with $k = 7$) is indicated by: $T/2$ at $t = t_{944}^* + T/2$; T at $t = t_{944}^* + T$; $3T/2$ at $t_{944}^* + 3T/2$; and $2T$ at $t_{944}^* + 2T$. Dark diamonds show s_J , s_N , and s_S ; dark triangles show s_1 , s_2 , and s_3 ; lighter diamonds show $s_J + T$, $s_N + T$, and $s_S + T$; and light triangles show $s_1 + T$, $s_2 + T$, and $s_3 + T$.

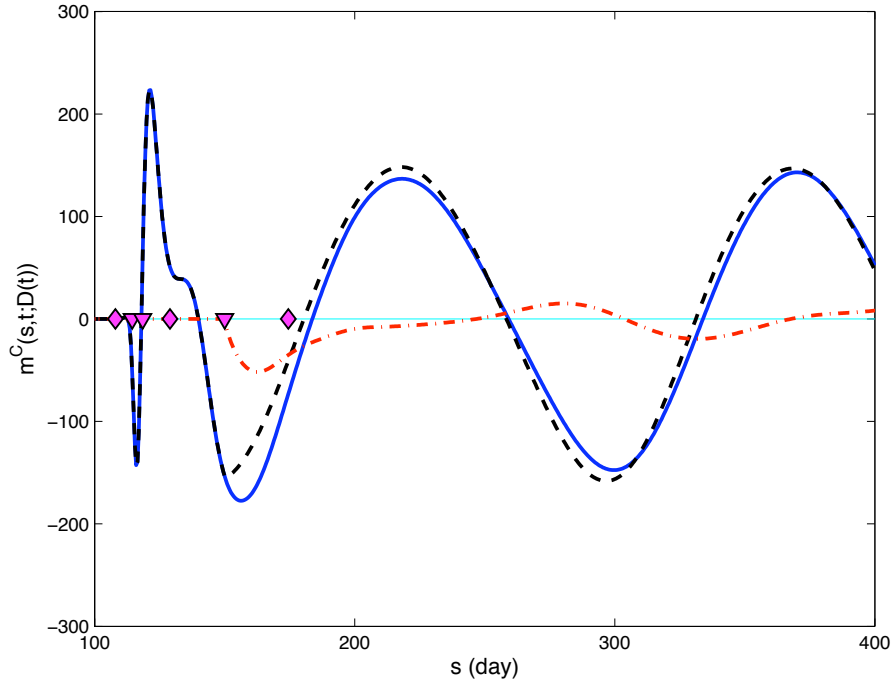


Fig. 6. Pseudo-lobes of $m^C(s, t; D(t))$ for the total transient transport (solid line; same as in Figure 5), $m^C(s, t; D^{cv}(t))$ by the circulating eddy vortices (dash line), and $m^C(s, t; D^{rw}(t))$ by the circulating eddy vortices (dash-dot line) at $t = t_{36}^* + kT$ (i.e., the end of $T^{[k]}$); the figure is made at t_{1095}^* using $k = 7$. Dark diamonds and dark triangles are the same as in Figure 5.

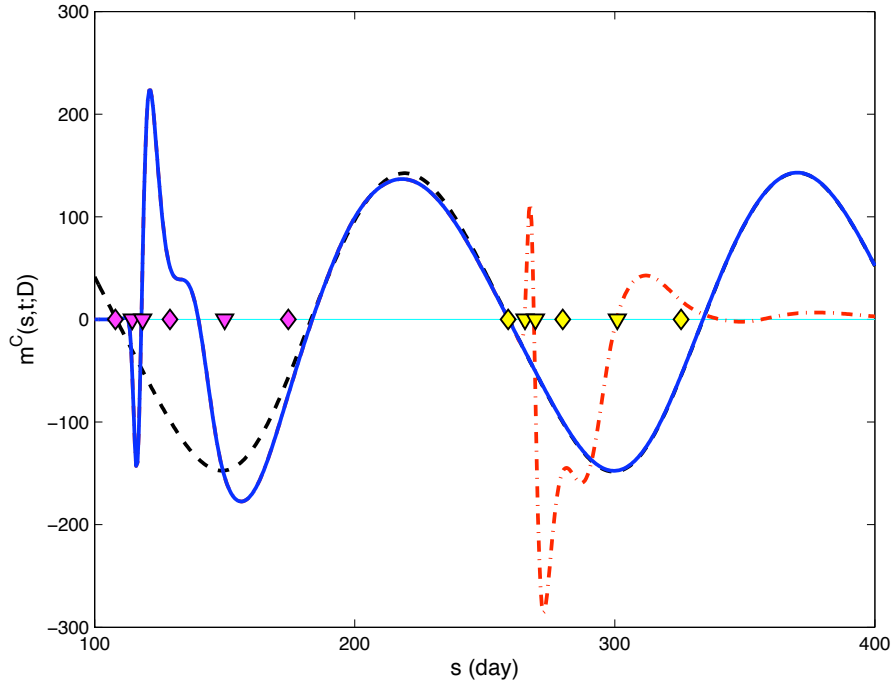


Fig. 7. Pseudo-lobes of $m^C(s, t; D(t))$ for the total transient transport (solid line; same as in Figures 5), $m^C(s, t; D^{[k]})$ for transport induced during $T^{[k]}$ (dash-dot line), $m^C(s, t; D^{\text{all}})$ for total transport (dash line) at $t = t_{36}^* + kT$ (i.e., the end of $T^{[k]}$); the figure is made at t_{1095}^* using $k = 7$. Diamonds and triangles are the same as in Figure 5.